PAPER

Check for updates

Temperature-dependent hydrogenation behaviour and hydrogen storage thermodynamics of $Mg_{0.9}In_{0.1}$ solid solution alloy

Yingyu Xu, Cong Peng and Qingan Zhang (ID) *

To clarify the hydrogen storage mechanism of Mg(In) solid solution, the hydrogenation and dehydrogenation characteristics of $Mg_{0.9}In_{0.1}$ alloy are systematically studied in this work. It is found that the $Mg_{0.9}In_{0.1}$ solid solution is first hydrogenated to Mg_3In and MgH_2 under a hydrogen atmosphere. The polymorphism of Mg_3In leads to different hydrogenation features of the solid solution in various temperature ranges. Consequently, the reversible dehydrogenation reactions have somewhat distinct enthalpy changes due to the different crystal structures of Mg_3In. When the hydrogenation temperature is not lower than 340 °C, Mg_3In can be further hydrogenated to $(Mg_{1-x}In_x)_3In$ and MgH_2. The hydrogenation reactions of both β'-Mg_3In and β-Mg_3In are also reversible although they have sloping hydrogenation and dehydrogenation plateaus in pressure–composition isotherms. This work provides new insights into the hydrogen storage mechanism of Mg(In) solid solution.

1. Introduction

Magnesium hydride (MgH_2) has been widely studied as a solid state hydrogen storage material with a hydrogen capacity of 7.6 wt%.[1,2] However, the practical applications of MgH_2 are still limited due to its high thermodynamic stability and slow desorption kinetics.[3,4] To reduce the thermodynamic stability, alloying Mg with other elements is usually used to destabilize the Mg–H bonds.[5] For example, Mg_2Ni can absorb hydrogen to form Mg_2NiH_4 with an absolute enthalpy change of 64 kJ mol^{-1} H$_2$ which is smaller than the value of 75 kJ mol^{-1} H$_2$ for pure Mg.[6] However, the reversible hydrogen capacity greatly decreases from 7.6 to 3.6 wt%. Another pathway is achieved by the reactions of MgH_2 with reactive elements, such as Si and Ge, to form Mg-based compounds.[7] In this case, MgH_2 can be destabilized to some extent but the hydrogenation–dehydrogenation kinetics is slowed down.[8] Thus more effective approaches should be adopted to simultaneously ensure high hydrogen capacity, fast desorption kinetics and suitable desorption thermodynamics.

Not long ago, Zhu proposed an interesting and effective approach to alter the desorption enthalpy of MgH_2 by the reversible formation of Mg(In) solid solution.[9] It was found that the $Mg_{0.95}In_{0.05}$ solid solution alloy had a reduced hydrogen absorption enthalpy of −68.1 kJ mol^{-1} H$_2$ and a reversible hydrogen capacity of 5.3 wt%.[9,10] Thereafter, the Mg(In) solid solution alloys have attracted more attention as one of the most promising hydrogen storage materials.[11–14] However, the previously reported results on the hydrogenation–dehydrogenation mechanism of Mg(In) solid solution alloys were ambiguous. Some researchers reported that the Mg(In) solid solution phase was hydrogenated to Mg_2In, β''-MgIn and MgH_2 at 300 °C, and further to the β phase and MgH_2 at 400 °C.[9,10] All the hydrogenated products can be reversibly dehydrogenated to the Mg(In) solid solution phase. Another group proposed that the Mg(In) solid solution phase was hydrogenated first to β'-Mg_3In and MgH_2, then to Mg_2In and MgH_2, and finally to β''-MgIn and MgH_2.[11,12] These hydrogenation reactions were also reversible during the subsequent dehydrogenation process. In a recent investigation, the authors suggested that the mechanism of the reversible hydrogenation–dehydrogenation reaction should be described as Mg(In) + H$_2$ ↔ MgH_2 + β'-Mg_3In.[13,14] Such differences in the hydrogenation mechanism of the Mg(In) solid solution might be related to different experimental conditions due to the complex phase relationship in the Mg-rich Mg-In system.[15]

According to the Mg-In phase diagram (see Fig. 1), the β phase with the disordered fcc A1-type structure can exist in a wide composition range from 23.2 to 93.5 at% In.[15] During slow cooling, the β phase will transform into the ordered L1$_2$-type (Cu$_3$Au-type) β' phase in space group $Pm\bar{3}m$ when the indium content is less than 39 at% and into the ordered L1$_0$-type (CuAu(I)-type) β'' phase in space group $P4/mmm$ as the indium content is about 39–59 at%.[15] When the composition is around 25 at% In, the ordering transformations from the disordered β-Mg_3In phase to the ordered L1$_2$-type β'-Mg_3In and further to the ordered 12R-type β_1-Mg_3In occur by slow

School of Materials Science and Engineering, Anhui University of Technology, Maanshan 243002, China. E-mail: qazhang@ahut.edu.cn
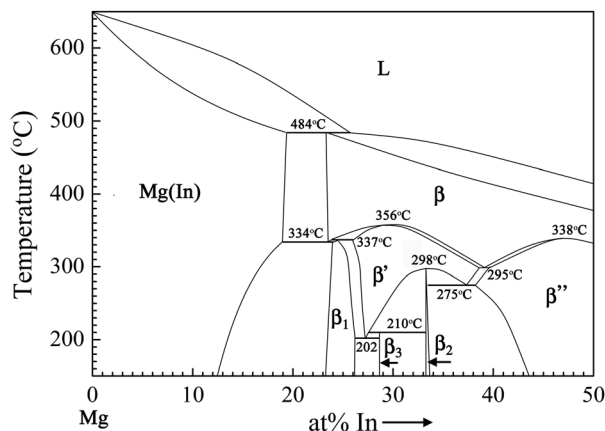
Fig. 1 Phase diagram of the Mg-rich Mg-In system redrawn from ref. 15.

cooling.[16] Hence, the complexity of phase transitions in the Mg-rich Mg-In system will inevitably result in various hydrogen-induced disproportionation reactions of the Mg(In) solid solution under different experimental conditions. To clarify the hydrogenation–dehydrogenation mechanism of the Mg(In) solid solution phase, the $Mg_{0.9}In_{0.1}$ alloy was selected as a research object in this work in view of the fact that the solubility limit of In in Mg is about 11 at% at room temperature.[15] Given the complexity in the hydrogenation reaction of Mg(In) solid solution, the hydrogenation–dehydrogenation behaviour of the Mg_3In alloy was studied first. Then the phase changes of the $Mg_{0.9}In_{0.1}$ alloy during hydrogen absorption and desorption were investigated. Finally, the hydrogen storage thermodynamics of the $Mg_{0.9}In_{0.1}$ alloy were studied systematically.

2. Experimental

2.1 Material preparation

Commercial magnesium (Acros, 99%) and indium (Innochem, 99.9%) bulks were used as raw materials. $Mg_{0.9}In_{0.1}$ and Mg_3In (atomic ratio) alloys were prepared by melting appropriate amounts of the pure metals in sealed quartz tubes under vacuum. Before preparation, the burning loss of Mg during melting was determined to be 20 wt% by trial-and-error. Thus extra Mg (20 wt%) was added to compensate for the burning loss. During the melting process, the quartz tubes filled with raw materials were heated to 750 °C at a rate of 5 °C min^{-1} and held for 10 minutes. After that, the ingots were homogenized by annealing at 300 °C for 24 hours. The annealed samples were polished to remove oxide films and then manually ground into 400-mesh powders in a glove box under a dry argon atmosphere for hydrogenation/dehydrogenation reactions and hydrogen absorption and desorption measurements.

2.2 Hydrogen absorption–desorption measurements

The isothermal hydrogenation and dehydrogenation reactions of the annealed $Mg_{0.9}In_{0.1}$ and Mg_3In alloys were carried out at

target temperatures under a hydrogen pressure of 7 MPa and vacuum, respectively. Pressure–composition (*P–C*) isotherms and isothermal hydrogenation and dehydrogenation curves of the annealed $Mg_{0.9}In_{0.1}$ alloy were measured using a Sieverts-type apparatus. Prior to the measurements, the $Mg_{0.9}In_{0.1}$ alloy was activated by two hydrogenation–dehydrogenation cycles at 350 °C.

2.3 Characterization

Elemental analyses of the alloys were performed on an inductively coupled plasma emission spectrometer (ICP, ICPS-7510 PLUS). The measured compositions were 90.4 at% Mg–9.6 at% In and 75.8 at% Mg–24.2 at% In, respectively, close to the nominal ones of $Mg_{0.9}In_{0.1}$ and Mg_3In alloys. The microstructure of the $Mg_{0.9}In_{0.1}$ alloy was observed using an optical microscope (MJ31, Mshot) and a scanning electron microscope (SEM, TESCAN MIRA3) equipped with an energy dispersive X-ray (EDX) spectroscope. For the observation, the sample was prepared by mechanical polishing and etching with a solution consisting of picric acid (2.5 g), acetic acid (5 ml), alcohol (40 ml) and water (10 ml). The microstructures of hydrogenated and dehydrogenated samples were observed using a transmission electron microscope (TEM, JEM-2011). The TEM samples were prepared by dispersing powders in tetrahydrofuran with ultrasonic vibration and then depositing the suspensions onto a copper grid. To identify the phase structures of all samples, powder X-ray diffraction (XRD) measurements were carried out using a Rigaku Miniflex-600C diffractometer with Cu Kα radiation at 40 kV and 15 mA. The XRD profiles were refined by the Rietveld method using RIETAN-2000.[17]

In situ XRD measurements of the annealed alloys during hydrogen absorption were performed using the HTHP-XRD-500 sample cell (Beijing Scistar Technol. Co. Ltd) with a silver holder and a beryllium window. During the *in situ* XRD measurements, the temperature was raised from 300 °C to 400 °C in steps of 10 °C and the hydrogen pressure was maintained at 4 MPa. In each step, the *in situ* XRD data of the Mg_3In sample were recorded after a two-hour holding period. For the $Mg_{0.9}In_{0.1}$ sample, the holding period time in each step was set to ten hours due to its slower hydrogenation kinetics.

3. Results and discussion

3.1 Hydrogenation and dehydrogenation behaviour of Mg_3In alloy

To clearly understand the hydrogenation characteristics of the Mg(In) solid solution phase, first we studied the hydrogenation behaviour of the Mg_3In alloy. Fig. 2a shows the Rietveld refinement of the XRD pattern for the annealed Mg_3In alloy. It can be seen that this sample has a single β-Mg_3In phase with a fcc-A1 structure in the space group $Fm\bar{3}m$. The lattice parameter can be determined to be a = 4.5165(6) Å. Generally, ordering transformations from β-Mg_3In to β′-Mg_3In and further to β$_1$-Mg_3In occur during slow cooling to temperatures below
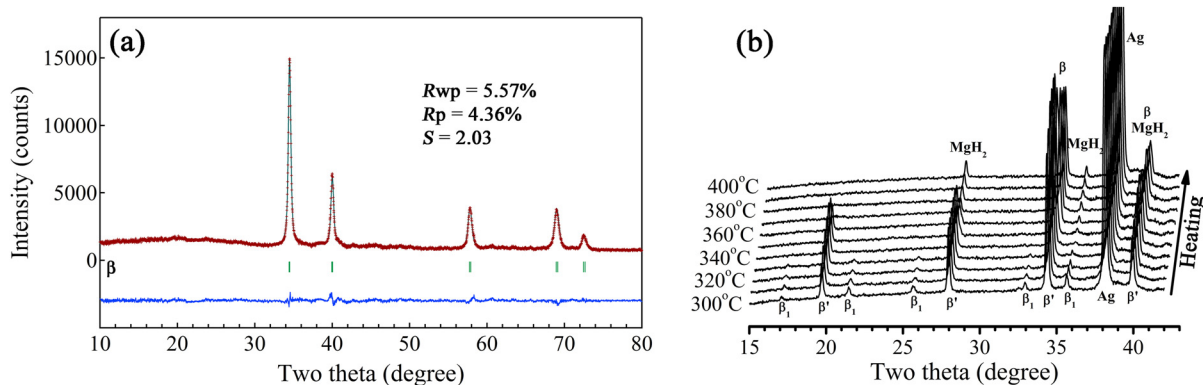
Fig. 2 (a) Rietveld refinement of the observed XRD patterns for annealed Mg_3In alloy and (b) *in situ* XRD patterns of the annealed Mg_3In alloy during the hydrogenation process (the Ag peak is from the sample holder).
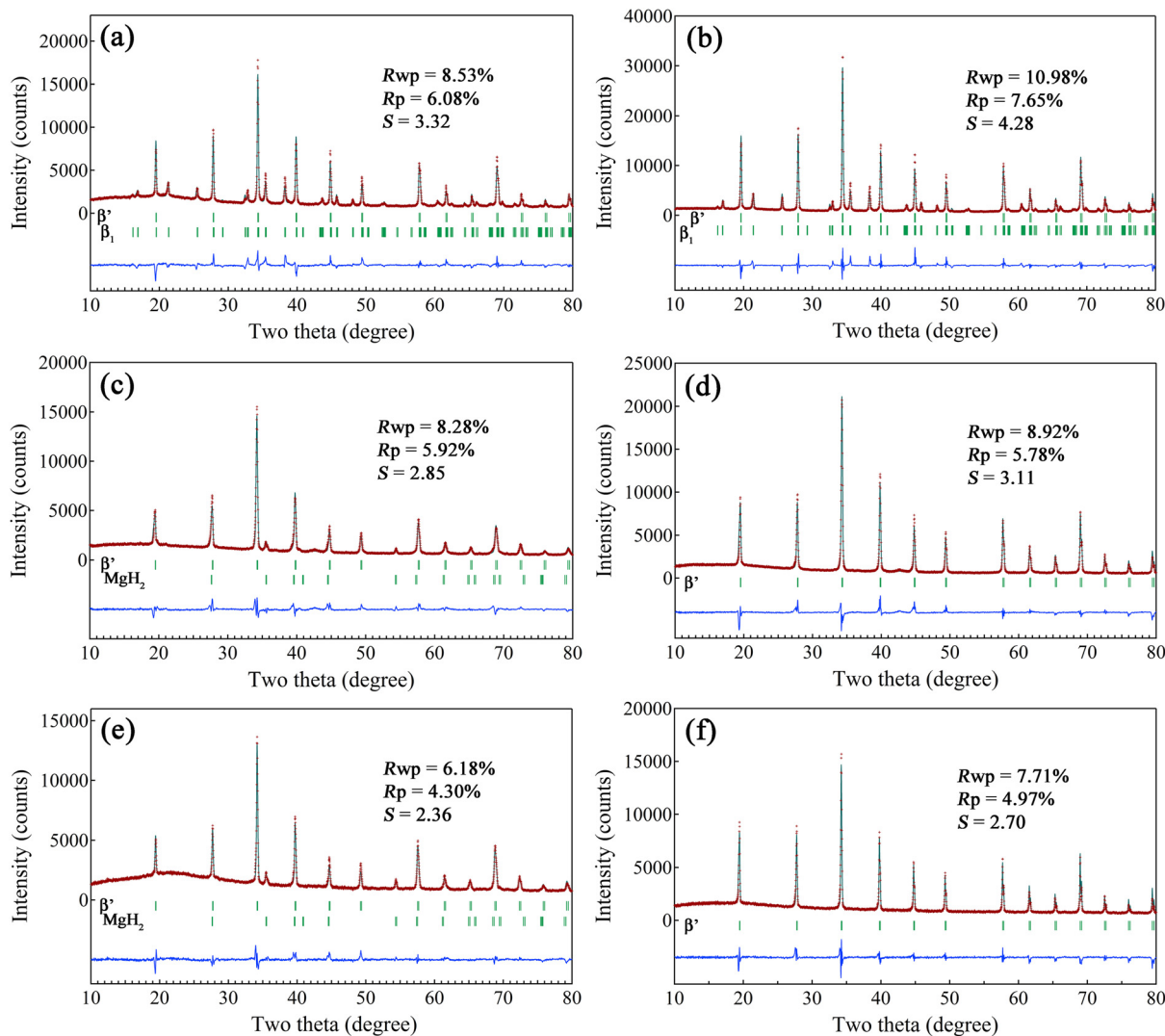

Fig. 3 Rietveld refinements of the observed XRD patterns for the Mg_3In samples hydrogenated and dehydrogenated at (a and b) 320, (c and d) 350 and (e and f) 390 °C for 10 hours.

340 °C.[15] In the present work, however, neither β′-Mg₃In nor β₁-Mg₃In was observed in the sample annealed at 300 °C for 24 h. This means that the ordering transformations of β-Mg₃In have very slow kinetics at 300 °C.

Fig. 2b shows the *in situ* XRD patterns of the annealed Mg₃In alloy during the heating process under a hydrogen pressure of 4 MPa. It can be seen that the diffraction peaks of both β′-Mg₃In and β₁-Mg₃In are present in the temperature range from 300 to 330 °C. As the temperature is raised to 340–360 °C, only the diffraction peaks of β′-Mg₃In and MgH₂ are observable. It is interesting that the peaks of β-Mg₃In reappear together with those of MgH₂ starting at 370 °C. This indicates that the hydrogenation of β-Mg₃In proceeds in three stages within the temperature range from 300 to 400 °C.

To further explore the transformation mechanism of the β-Mg₃In phase under a hydrogen atmosphere, isothermal hydrogenation and dehydrogenation reactions were carried out. Fig. 3a shows the Rietveld refinement of the XRD pattern for the Mg₃In sample hydrogenated at 320 °C for 10 hours. It can be seen that the hydrogenated sample consists of β′-Mg₃In and β₁-Mg₃In phases, demonstrating that the ordering transformations of Mg₃In occurred during the hydrogenation process. Thus the overall reaction within the temperature range of 300–330 °C can be expressed as

$$\beta\text{-Mg}_3\text{In} \rightarrow \beta'\text{-Mg}_3\text{In} + \beta_1\text{-Mg}_3\text{In} \tag{1}$$
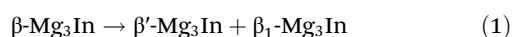
Such a hydrogen-induced ordering phenomenon is similar to that observed in ErNi₂ where the ordering transformation

from a MgCu₂-type structure to a TmNi₂-type superstructure easily occurred by hydrogenation at 25 °C.[18] This is because the formation and migration of vacancies and rearrangement of metal atoms can be greatly promoted by dissolved hydrogen.[19,20] After dehydrogenating the hydrogenated Mg₃In sample at 320 °C for 10 hours, the XRD pattern almost remains unchanged compared with that of the hydrogenated sample (see Fig. 3b). This means that reaction (1) is irreversible during the dehydrogenation process at 320 °C. This is because there is a certain amount of hydrogen atoms remaining inside
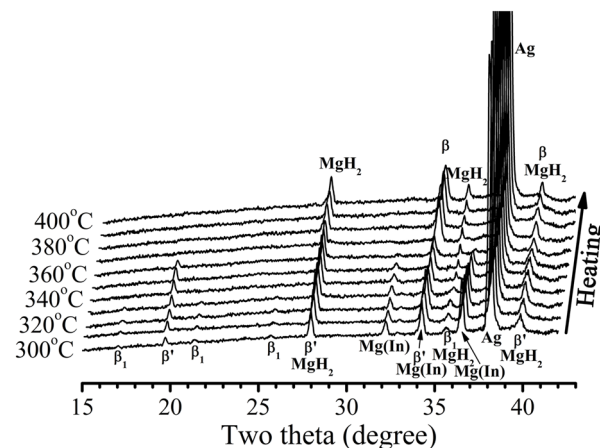

Fig. 5 *In situ* XRD patterns of Mg₀.₉In₀.₁ alloy during the hydrogenation process (the Ag peak is from the sample holder).
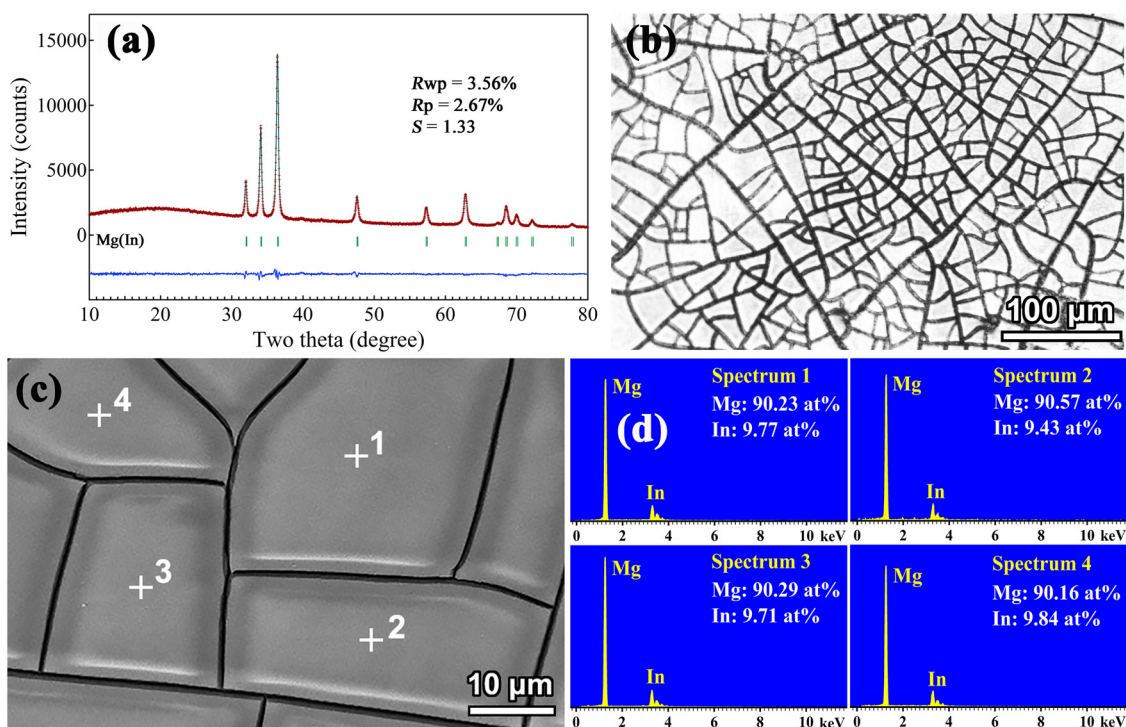

Fig. 4 (a) XRD patterns, (b) optical morphology, (c) SEM image and (d) EDX spectra for annealed Mg₀.₉In₀.₁ alloy.

the β′-Mg$_3$In and β$_1$-Mg$_3$In phases after dehydrogenation, stabilizing the ordered structures.[18,20]

Fig. 3c shows the Rietveld refinement of the XRD pattern for the Mg$_3$In sample hydrogenated at 350 °C for 10 h. Obviously, the hydrogenated sample is composed of β′ and MgH$_2$ phases. In the ideal Cu$_3$Au-type β′-Mg$_3$In structure, Mg and In atoms occupy the 3c site (0, 1/2, 1/2) and 1a site (0, 0, 0), respectively. However, the real β′ phase exists in a composition range of 26–38.8 at% In because indium atoms can partially occupy the 3c site of Mg.[15] In the present work, the occupancy factors of Mg and In atoms in the 3c site were determined to be 0.91 and 0.09, respectively, by the Rietveld refinement of the XRD pattern. Thus the β′ phase in the hydrogenated sample can be denoted as β′-(Mg$_{0.91}$In$_{0.09}$)$_3$In. This means that the β-Mg$_3$In phase first transforms into the ordered β′-Mg$_3$In and further decomposes to β′-(Mg$_{0.91}$In$_{0.09}$)$_3$In and MgH$_2$ during the isothermal hydrogenation at 350 °C. The overall hydrogenation reaction can be written as

$$\beta\text{-Mg}_3\text{In} + \text{H}_2 \rightarrow \beta'\text{-(Mg}_{1-x}\text{In}_x)_3\text{In} + \text{MgH}_2 \quad (2)$$
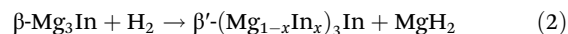
Fig. 3d shows the XRD pattern of the Mg$_3$In sample dehydrogenated at 350 °C for 10 hours. It can be seen that only the β′-Mg$_3$In phase appears in the dehydrogenated sample. Thus the dehydrogenation reaction can be expressed as

$$\beta'\text{-(Mg}_{1-x}\text{In}_x)_3\text{In} + \text{MgH}_2 \rightarrow \beta'\text{-Mg}_3\text{In} + \text{H}_2 \quad (3)$$
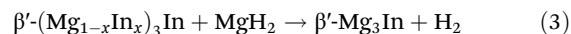
Fig. 3e and f show the XRD patterns of the Mg$_3$In samples hydrogenated and dehydrogenated at 390 °C for 10 h, which are similar to those of the samples hydrogenated and dehydrogenated at 350 °C for 10 h. The composition of the β′ phase in the hydrogenated sample can be determined to be β′-(Mg$_{0.86}$In$_{0.14}$)$_3$In by Rietveld analysis. However, the *in situ* XRD
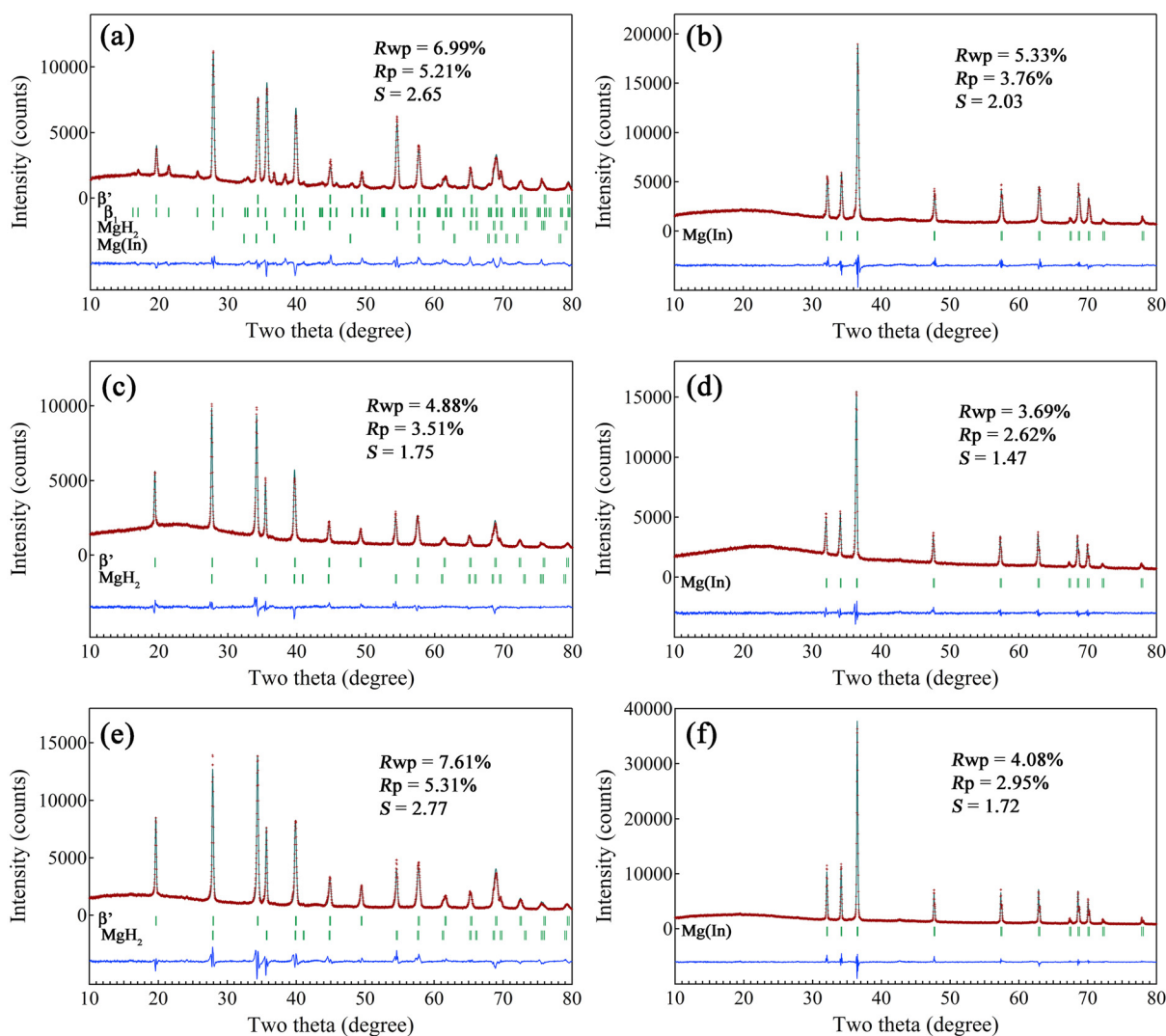

Fig. 6 Rietveld refinements of the observed XRD patterns for the Mg$_{0.9}$In$_{0.1}$ samples hydrogenated and dehydrogenated at (a and b) 320 °C for 50 hours, (c and d) 350 °C for 50 hours, and (e and f) 390 °C for 20 hours.

patterns clearly indicate the existence of β and MgH_2 phases as the hydrogenation products at 390 °C (see Fig. 2b). These results demonstrate that the β phase in the hydrogenated and dehydrogenated samples quickly transformed into the β′ phase in the subsequent cooling process. This is because the ordering transformation of the β phase to the β′ phase proceeds very fast due to a large number of crystal defects including vacancies and interstitial H atoms.[20] Hence, the reversible reactions at 390 °C can be expressed as

$$\beta\text{-}Mg_3In + H_2 \ \leftrightarrow \ \beta\text{-}(Mg_{1-x}In_x)_3In + MgH_2 \qquad (4)$$
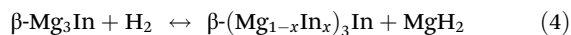
3.2 Hydrogenation and dehydrogenation mechanism of Mg (In) solid solution

Fig. 4a shows the Rietveld refinement of the XRD pattern for the annealed $Mg_{0.9}In_{0.1}$ alloy. It can be seen that a single Mg (In) solid solution phase is present. The lattice parameters were determined to be $a = 3.3017(2)$ Å and $c = 5.2201(2)$ Å. Compared with the values $a = 3.2125(5)$ Å and $c = 5.2132(8)$ Å for pure Mg,[21] the parameter a decreases but the parameter c increases due to partial substitution by In. Thus the axial ratio c/a increases from 1.623 to 1.630 and the unit cell volume decreases from 46.59 to 46.34 Å^3, similar to the results reported previously.[22] The optical morphology in Fig. 4b shows that the alloy has an average grain size of 20 μm. The SEM/EDX analysis (Fig. 4c and d) indicates that Mg and In elements are uniformly distributed without composition segregation, and the average composition is 90.3 at% Mg–9.7 at% In, which is close to the nominal one.
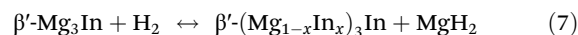
Fig. 5 shows the *in situ* XRD patterns of the $Mg_{0.9}In_{0.1}$ alloy during the heating process under a hydrogen pressure of 4 MPa. Because the hydrogenation reaction of $Mg_{0.9}In_{0.1}$ alloy proceeds slowly, the diffraction peaks of the Mg(In) solid solution phase are present until the temperature reaches 360 °C. Despite this, it is clear that the hydrogenation of the Mg(In) solid solution phase also has three distinguishable stages. When the temperature ranges from 300 to 330 °C, β′-Mg_3In, $β_1$-Mg_3In and MgH_2 are formed as the products of hydrogenation. Upon increasing the temperature to 340–360 °C, $β_1$-Mg_3In disappears but the β′ and MgH_2 phases are retained. As the temperature is further raised to 370 °C, only the peaks of the β phase and MgH_2 are observable.

Fig. 6a shows the Rietveld refinement of the XRD pattern for the $Mg_{0.9}In_{0.1}$ alloy hydrogenated at 320 °C for 50 hours, indicating the coexistence of β′-Mg_3In, $β_1$-Mg_3In, MgH_2 and remaining Mg(In). When the hydrogenated sample was dehydrogenated at 320 °C for 50 hours, the Mg(In) solid solution phase was reversibly formed (see Fig. 6b). Thus, the hydrogenation and dehydrogenation reactions of Mg(In) in the temperature range from 300 to 330 °C can be written as
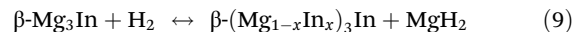
$$Mg(In) + H_2 \ \leftrightarrow \ \beta'\text{-}Mg_3In + \beta_1\text{-}Mg_3In + MgH_2 \qquad (5)$$
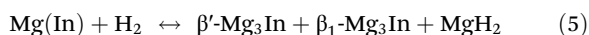
When the $Mg_{0.9}In_{0.1}$ alloy was hydrogenated at 350 °C for 50 hours, the β′ and MgH_2 phases were generated (see Fig. 6c). The composition of the β′ phase was determined to be

$(Mg_{0.92}In_{0.08})_3In$ by Rietveld refinement. Likewise, the β′-$(Mg_{0.92}In_{0.08})_3In$ and MgH_2 phases can be reversibly transformed into Mg(In) during subsequent dehydrogenation (see Fig. 6d). According to Fig. 5, 6c and d, the hydrogenation and dehydrogenation reactions of Mg(In) in the range of 340–360 °C can be expressed as

$$Mg(In) + H_2 \ \leftrightarrow \ \beta'\text{-}Mg_3In + MgH_2 \qquad (6)$$

$$\beta'\text{-}Mg_3In + H_2 \ \leftrightarrow \ \beta'\text{-}(Mg_{1-x}In_x)_3In + MgH_2 \qquad (7)$$

The XRD patterns of $Mg_{0.9}In_{0.1}$ samples hydrogenated and dehydrogenated at 390 °C for 20 hours are shown in Fig. 6e and f, respectively. Similarly, β′ and MgH_2 are detectable in the hydrogenated sample and Mg(In) is observable in the dehydrogenated sample. The composition of the β′ phase can be calculated to be $(Mg_{0.85}In_{0.15})_3In$. For the same reasons as mentioned above for Mg_3In alloy, the β′-$(Mg_{0.85}In_{0.15})_3In$ phase was formed from the hydrogenation product β-$(Mg_{0.85}In_{0.15})_3In$ during the cooling process. Hence, the hydrogenation and dehydrogenation reactions of Mg(In) in the range from 370 to 400 °C can be written as

$$Mg(In) + H_2 \ \leftrightarrow \ \beta\text{-}Mg_3In + MgH_2 \qquad (8)$$

$$\beta\text{-}Mg_3In + H_2 \ \leftrightarrow \ \beta\text{-}(Mg_{1-x}In_x)_3In + MgH_2 \qquad (9)$$

To further confirm this, the microstructures of hydrogenated and dehydrogenated $Mg_{0.9}In_{0.1}$ samples were observed by TEM (see Fig. 7). Evidently, the hydrogenated sample consists of β′ and MgH_2 phases, and the dehydrogenated sample is composed of a single phase Mg(In).
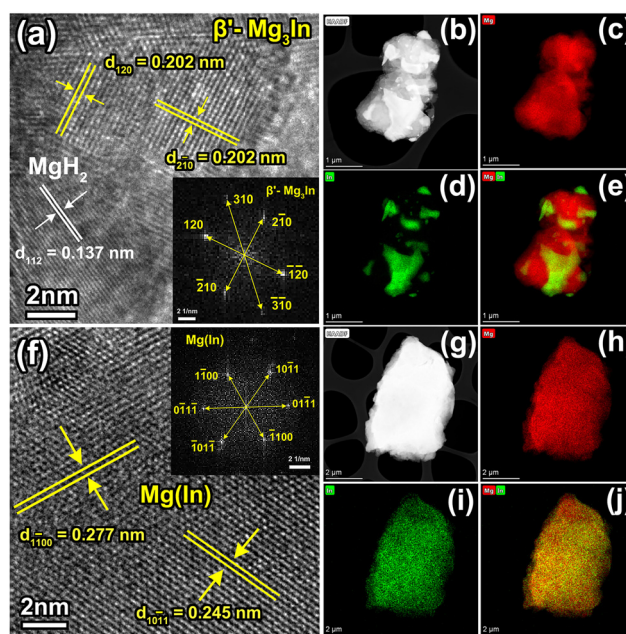

Fig. 7 HRTEM images, HAADF-STEM images and the corresponding EDX elemental mappings of the $Mg_{0.9}In_{0.1}$ samples (a–e) hydrogenated and (f–j) dehydrogenated at 390 °C.

It should be noted that neither β_2-Mg_2In nor β''-MgIn was observed in the hydrogenated samples. This result might be related to the slow kinetics of hydrogen-induced decomposition. Fig. 8 shows the isothermal hydrogenation and dehydrogenation curves at different temperatures. It can be seen that the hydrogenation reaction takes 20 hours even at 390 °C. This is because the hydrogen-induced decomposition of Mg (In) requires long-range diffusion of In atoms (see Fig. 7d). In contrast, the hydrogenation kinetic rate of mechanically alloyed Mg(In) alloy becomes faster due to its nanoscale
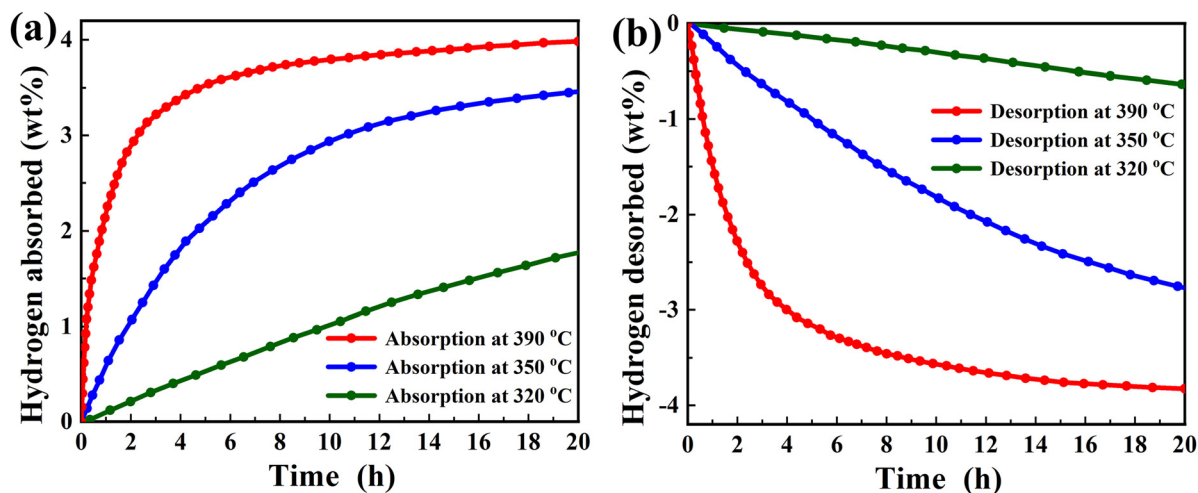

Fig. 8 (a) Hydrogenation and (b) dehydrogenation curves of the $Mg_{0.9}In_{0.1}$ alloy at different temperatures.
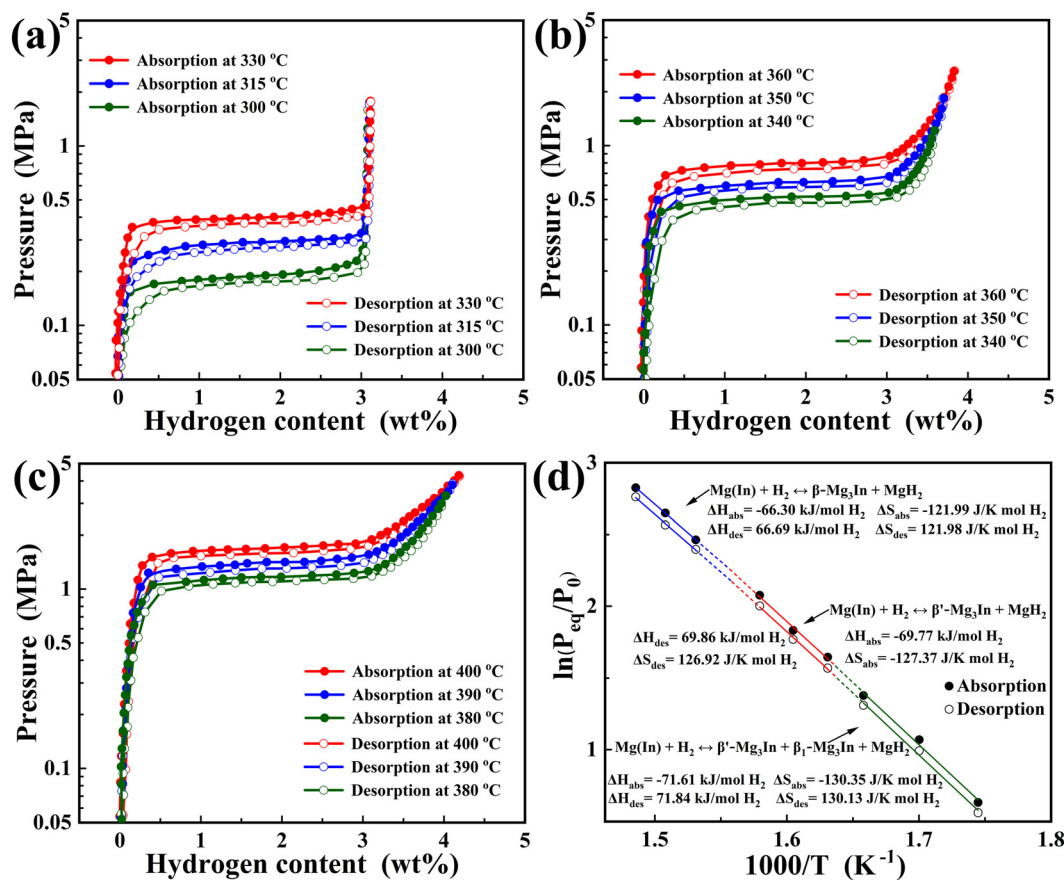

Fig. 9 (a–c) *P–C* isotherms of hydrogen absorption and desorption at different temperatures and (d) van't Hoff plots for the flat plateaus of $Mg_{0.9}In_{0.1}$.

microstructure.[10,12] Once the composition of the hydrogenation product enters the β″ phase region, non-stoichiometric β″-MgIn can be formed (see Fig. 1).

3.3 Hydrogenation and dehydrogenation thermodynamics

Fig. 9a presents the *P–C* isotherms of hydrogen absorption and desorption for the activated $Mg_{0.9}In_{0.1}$ sample at 300, 315 and 330 °C. It can be seen that only one plateau is visible on each curve, corresponding to reaction (5). However, two plateaus (one is flat and the other is sloping) can be observed on each curve at 340, 350 and 360 °C (see Fig. 9b), relevant to reactions (6) and (7), respectively. Similarly, two plateaus corresponding to reactions (8) and (9) are also found in the *P–C* isotherms at 380, 390 and 400 °C (see Fig. 9c). These results also demonstrate that the Mg(In) solid solution phase has various hydrogenation and dehydrogenation mechanisms in different temperature ranges.

The van't Hoff plots for the flat plateaus are displayed in Fig. 9d. Consequently, the dehydrogenation enthalpies for reactions (5), (6) and (8) can be calculated to be 71.84, 69.86 and 66.69 kJ mol⁻¹ H_2, respectively. Obviously, these dehydrogenation enthalpies are smaller than the value of 75 kJ mol⁻¹ H_2 for MgH_2.[6] This means that indium doping can improve the dehydrogenation thermodynamics, which provides a possible pathway to achieving the US-DOE's goals.[23] The thermodynamic destabilization of MgH_2 is related to the reaction of the hydride with Mg_3In forming Mg(In) solid solution upon dehydrogenation.[9,12,24] However, the present work indicates that different crystal structures of Mg_3In result in various degrees of destabilization. This is because the enthalpy of formation for Mg_3In is associated with the change in stacking sequence ($\beta_1 \rightarrow \beta'$) and the order–disorder phase transition ($\beta' \rightarrow \beta$).[15,16,25]

As for the sloping plateaus of reactions (7) and (9), the slopes indicate different portions of hydrogen-induced Mg_3In decomposition at various pressures.[26] The decomposition reaction of Mg_3In might not be complete yet due to slow kinetics when the measurements of hydrogenation isotherms were terminated. Thus it is difficult to accurately calculate the enthalpy changes of reactions (7) and (9) by taking the equilibrium pressures from the midpoints of sloping plateaus. In the present case, the sample is composed of β-$(Mg_{1-x}In_x)_3In$ and MgH_2 after the measurement of hydrogenation performance at 400 °C. However, further increasing the hydrogenation temperature will result in the occurrence of partial melting as the composition of β-$(Mg_{1-x}In_x)_3In$ reaches the solidus line (see Fig. 1), which makes its hydrogenation behaviour more complicated. Thus further investigations are needed to understand the de/hydrogenation feature of the β phase on the basis of enhancement of the kinetics.[27,28]

4. Conclusions

In conclusion, the $Mg_{0.9}In_{0.1}$ solid solution alloy has various hydrogenation mechanisms at different temperature ranges. The β_1-Mg_3In, β'-Mg_3In and MgH_2 phases can be formed in

the temperature range from 300 to 330 °C. As the temperature increases to the range of 340–360 °C, the solid solution phase is firstly hydrogenated to β'-Mg_3In and MgH_2, and β'-Mg_3In is then hydrogenated to β'-$(Mg_{1-x}In_x)_3In$ and MgH_2. With increasing temperature up to 370 °C, β-Mg_3In and MgH_2 are formed initially as hydrogenation products and the β-Mg_3In phase is further hydrogenated to β-$(Mg_{1-x}In_x)_3In$ and MgH_2. All the hydrogenation reactions are reversible upon dehydrogenation. The dehydrogenation enthalpies of MgH_2 + Mg_3In are 71.84, 69.86 and 66.69 kJ mol⁻¹ H_2, respectively, in the three temperature ranges. The degree of thermodynamic destabilization by forming Mg(In) solid solution is associated with the crystal structures of Mg_3In.

Author contributions

Yingyu Xu: investigation, data processing and writing. Cong Peng: review and editing. Qingan Zhang: conceptualization, supervision, review and funding acquisition.

Data availability

The authors confirm that the data supporting the findings of this study are available within the article.

Conflicts of interest

There are no conflicts to declare.

Acknowledgements

References

1 V. A. Yartys, M. V. Lototskyy, E. Akiba, R. Albert, V. E. Antonov, J. R. Ares, M. Baricco, N. Bourgeois, C. E. Buckley, J. M. Bellosta von Colbe, J. C. Crivello, F. Cuevas, R. V. Denys, M. Dornheim, M. Felderhoff, D. M. Grant, B. C. Hauback, T. D. Humphries, I. Jacob, T. R. Jensen, P. E. de Jongh, J. M. Joubert, M. A. Kuzovnikov, M. Latroche, M. Paskevicius, L. Pasquini, L. Popilevsky, V. M. Skripnyuk, E. Rabkin, M. V. Sofianos, A. Stuart, G. Walker, H. Wang, C. J. Webb and M. Zhu, *Int. J. Hydrogen Energy*, 2019, **44**, 7809–7859.
2 J. Zhang, Y. Zhu, L. Yao, C. Xu, Y. Liu and L. Li, *J. Alloys Compd.*, 2019, **782**, 796–823.
3 I. P. Jain, C. Lal and A. Jain, *Int. J. Hydrogen Energy*, 2010, **35**, 5133–5144.

4   B. Bogdanovic, K. Bohmhammel, B. Christ, A. Reiser, K. Schlichte, R. Vehlen and U. Wolf, *J. Alloys Compd.*, 1999, **282**, 84–92.

5   A. K. Singh, A. K. Singh and O. N. Srivastava, *J. Alloys Compd.*, 1995, **227**, 63–68.

6   J. J. Reilly and R. H. Wiswall, *Inorg. Chem.*, 1968, **7**, 2254–2256.

7   J. J. Vajo, F. Mertens, C. C. Ahn, R. C. Bowman Jr. and B. Fultz, *J. Phys. Chem. B*, 2004, **108**, 13977–13983.

8   J. Zhang, Z. Li, F. Cuevas and M. Latroche, *J. Phys. Chem. C*, 2014, **118**, 21889–21895.

9   H. C. Zhong, H. Wang, J. W. Liu, D. L. Sun and M. Zhu, *Scr. Mater.*, 2011, **65**, 285–287.

10 H. Wang, H. Zhong, L. Ouyang, J. Liu, D. Sun, Q. Zhang and M. Zhu, *J. Phys. Chem. C*, 2014, **118**, 12087–12096.

11 C. Zhou, Z. Z. Fang, J. Lu and X. Zhang, *J. Am. Chem. Soc.*, 2013, **135**, 10982–10985.

12 C. Zhou, Z. Z. Fang, J. Lu, X. Luo, C. Ren, P. Fan, Y. Ren and X. Zhang, *J. Phys. Chem. C*, 2014, **118**, 11526–11535.

13 D. Khan, J. Zou, S. Panda and W. Ding, *J. Phys. Chem. C*, 2020, **124**, 9685–9695.

14 Z. Ma, Z. Huang, Z. Li, G. Chen, Y. Li, W. Zhu, W. Zhao, H. Ji, H. Fang, W. Wen, W. Yin and J. Zou, *Energy Storage Mater.*, 2023, **56**, 432–442.

15 A. A. Nayeb-Hashemi and J. B. Clark, *Bull. Alloy Phase Diagrams*, 1985, **6**, 149–160.

16 Y. Watanabe, *Acta Metall.*, 1975, **23**, 691–696.

17 F. Izumi and T. Ikeda, *Mater. Sci. Forum*, 2000, **321**, 198–203.

18 Q. A. Zhang, Z. Q. Dong and S. C. Xie, *J. Alloys Compd.*, 2015, **626**, 189–193.

19 J. Bloch, O. Levy, B. Pejova, J. Jacob, S. Curtarolo and B. Hjorvarsson, *Phys. Rev. Lett.*, 2012, **108**, 215503.

20 M. Yamauchi, K. Okubo, T. Tsukuda, K. Kato, M. Takata and S. Takeda, *Nanoscale*, 2014, **6**, 4067–4071.

21 P. Karen, A. Kjekshus, Q. Huang and V. L. Karen, *J. Alloys Compd.*, 1999, **282**, 72–75.

22 F. W. von Batchelder and R. F. Raeuchle, *Phys. Rev. Lett.*, 1957, **105**, 59–61.

23 C. Li, W. Yang, H. Liu, X. Liu, X. Xing, Z. Gao, S. Dong and H. Li, *Angew. Chem., Int. Ed.*, 2024, **63**, e202320151.

24 J. J. Vajo and G. L. Olson, *Scr. Mater.*, 2007, **56**, 829–834.

25 T. Hirata, *Trans. Jpn. Inst. Met.*, 1971, **12**, 375–377.

26 J. W. Larsen and B. R. Livesay, Hydriding kinetics of SmCo5, *J. Less-Common Met.*, 1980, **73**, 79–88.

27 C. Peng, Y. Li and Q. Zhang, *Scr. Mater.*, 2024, **248**, 116149.

28 S. Guemou, D. Gao, F. Wu, J. Zheng, T. Wei, Z. Yao, D. Shang and L. Zhang, *Dalton Trans.*, 2023, **52**, 609–620.